Intraretinal Hyper-Reflective Foci Are Almost Universally Present and Co-Localize With Intraretinal Fluid in Diabetic Macular Edema

Esther L. von Schulthess,[1,] Andreas Maunz,[1] Usha Chakravarthy,[2] Nancy Holekamp,[1,3] Daniel Pauleikhoff,[4] Katie Patel,[5] Isabel Bachmeier,[1] Siqing Yu,[1] Yaniv Cohen,[1] Mahnaz Parian Scherb,[1] Ian L. Jones,[1] Kara Gibson,[5] Jeffrey R. Willis,[6] Carl Glittenberg,[1] Rishi P. Singh,[7] and Sascha Fauser[1]

[1]Roche Pharma Research and Early Development, Therapeutic Modalities, Roche Innovation Center Basel, F. Hoffmann-La Roche Ltd., Basel, Switzerland
[2]Queen's University of Belfast, Royal Victoria Hospital, Belfast, United Kingdom
[3]Pepose Vision Institute, Chesterfield, Missouri, United States
[4]Augenzentrum am St. Franziskus Hospital, Münster, Germany
[5]Roche Products Ltd., Welwyn Garden City, United Kingdom
[6]Genentech, Inc., South San Francisco, California, United States
[7]Center for Ophthalmic Bioinformatics, Cole Eye Institute, Cleveland Clinic, Cleveland, Ohio, United States

Correspondence: Esther L. von Schulthess, Roche Pharma Research and Early Development, Therapeutic Modalities, Roche Innovation Center Basel, F. Hoffmann-La Roche Ltd., Grenzacherstrasse 124, Basel CH-4070, Switzerland; esther.von_schulthess@roche.com.

ELS and AM contributed equally to this work and should be considered first co-authors.

Received: October 26, 2023
Accepted: April 28, 2024
Published: May 17, 2024

Citation: von Schulthess EL, Maunz A, Chakravarthy U, et al. Intraretinal hyper-reflective foci are almost universally present and co-localize with intraretinal fluid in diabetic macular edema. *Invest Ophthalmol Vis Sci.* 2024;65(5):26. https://doi.org/10.1167/iovs.65.5.26

Purpose. In diabetic macular edema (DME), hyper-reflective foci (HRF) has been linked to disease severity and progression. Using an automated approach, we aimed to investigate the baseline distribution of HRF in DME and their co-localization with cystoid intraretinal fluid (IRF).

Methods. Baseline spectral-domain optical coherence tomography (SD-OCT) volume scans ($N = 1527$) from phase III clinical trials YOSEMITE (NCT03622580) and RHINE (NCT03622593) were segmented using a deep-learning–based algorithm (developed using B-scans from BOULEVARD NCT02699450) to detect HRF. The HRF count and volume were assessed. HRF distributions were analyzed in relation to best-corrected visual acuity (BCVA), central subfield thickness (CST), and IRF volume in quartiles, and Diabetic Retinopathy Severity Scores (DRSS) in groups. Co-localization of HRF with IRF was calculated in the central 3-mm diameter using the en face projection.

Results. HRF were present in most patients (up to 99.7%). Median (interquartile range [IQR]) HRF volume within the 3-mm diameter Early Treatment Diabetic Retinopathy Study ring was 1964.3 (3325.2) pL, and median count was 64.0 (IQR = 96.0). Median HRF volumes were greater with decreasing BCVA (nominal $P = 0.0109$), and increasing CST (nominal $P < 0.0001$), IRF (nominal $P < 0.0001$), and DRSS up to very severe nonproliferative diabetic retinopathy (nominal $P < 0.0001$). HRF co-localized with IRF in the en face projection.

Conclusions. Using automated HRF segmentation of full SD-OCT volumes, we observed that HRF are a ubiquitous feature in DME and exhibit relationships with BCVA, CST, IRF, and DRSS, supporting a potential link to disease severity. The spatial distribution of HRF closely followed that of IRF.

Keywords: co-localization, deep learning, diabetic macular edema (DME), hyper-reflective foci (HRF), spectral-domain optical coherence tomography (SD-OCT)

Diabetic macular edema (DME) is a multifactorial disease,[1–3] with a significant inflammatory component.[4–7] Although treatment with antivascular endothelial growth factor (VEGF) has improved outcomes considerably,[8,9] the initial gains in visual acuity decline over time,[10] and a significant proportion of patients show persistent retinal thickening and fluid accumulation despite consistent long-term treatment.[11] In order to improve patient outcomes, disease-specific biomarkers linked to disease severity and progression are needed to better understand the pathophysiology of DME and to evaluate the benefit of additional modes of action that address factors beyond VEGF.

Hyper-reflective foci (HRF) have been proposed as a biomarker of disease severity and progression in DME.[12–15] HRF are small, distinct objects that generate a highly reflective signal on spectral-domain optical coherence tomography (SD-OCT).[16] They are present in multiple retinal diseases, including DME, neovascular age-related macular degeneration, retinal vein occlusion, and uveitic macu-

lar edema,[17,18] but likely have differing, disease-specific origins.[12]

In DME, there are two main hypotheses on the morphological correlate of HRF detected by SD-OCT. The first proposes that HRF are activated microglia or infiltrating leukocytes, thus representing a retinal inflammatory response.[19–22] The second hypothesis suggests that HRF are protein and/or lipid exudates resulting from the breakdown of the blood-retinal barrier.[16,17,23,24] There have also been studies showing co-localization of intraretinal hyperreflective material with intraretinal fluid cysts.[25] Because these hypotheses are not mutually exclusive, and are both related to vascular instability, some groups have also discussed the potential of both hypotheses applying concurrently, with smaller HRF (≤30 µm) proposed to correspond to inflammatory cells and larger objects (>30 µm) representing macromolecular exudates.[14,26] Histological studies on HRF are currently still lacking in DME, and are necessary to confirm these hypotheses.

Past studies, all using manual assessment, have come to inconsistent conclusions on whether the presence or number of HRF are predictive of visual outcome following treatment, although a greater number of studies found that HRF at baseline were predictive of a poor visual outcome.[27] Better consensus exists for response to treatment, with studies largely agreeing that treatment with either intravitreal anti-VEGF or steroids reduces the number of HRF in patients with DME; some studies showed a greater reduction with steroids versus anti-VEGF, whereas others did not find a difference.[27]

The aim of this work was to develop and assess the performance of a deep-learning–based algorithm to quantify HRF, investigate the baseline distribution of HRF within the retina and whether there is a link to disease severity, and determine whether HRF co-localize with cystoid IRF in patients with DME.

Materials and Methods

Patient Population

YOSEMITE (ClinicalTrials.gov identifier, NCT03622580) and RHINE (NCT03622593) were identical, randomized, double-masked, phase III clinical trials that assessed the safety, efficacy, and durability of faricimab compared with aflibercept in treatment-naïve and previously treated eyes with center-involving DME.[28,29] For the current post hoc analysis, baseline data from all arms of YOSEMITE and RHINE were pooled.

BOULEVARD (ClinicalTrials.gov identifier, NCT02699450) was a randomized, double-masked, phase II clinical trial, which compared the safety and efficacy of faricimab to ranibizumab in treatment-naïve and previously treated patients with center-involving DME.[30]

For all three studies, the study protocols were approved by respective institutional review boards, and the trials were conducted in accordance with Good Clinical Practice guidelines and the tenets of the Declaration of Helsinki. All patients provided written informed consent, including consent for secondary data use, before they enrolled in the study.

Data Selection

Study eyes of participants from phase III YOSEMITE and RHINE studies with Spectralis (Heidelberg Engineering, Heidelberg, Germany) volume scans (97 B-scans, with scan areas of 32.2 mm^2, 34.5 mm^2, and 37.4 mm^2 for the 10th, 50th, and 90th percentile, respectively) at the baseline visit were included in the analysis ($N = 1527$) and segmented with the model described below. Volumes acquired on Zeiss ($N = 150$) and Topcon ($N = 3$) devices were excluded in order to obtain a homogenous data set.

HRF Segmentation Model

Overview. We used a subset of manually annotated SD-OCT retinal B-scans (Spectralis) acquired from eyes of participants included in the BOULEVARD study to develop the HRF-segmentation model described in detail below. This algorithm was subsequently used on the baseline SD-OCT volume scans (Spectralis) from participants in the YOSEMITE and RHINE studies to automatically segment HRF across all B-scans (see Supplementary Fig. S1).

HRF Definition. HRF were defined as distinct bright dots of similar reflectivity to the retinal pigment epithelium (RPE) on SD-OCT. A range of upper size limits have been reported in the literature, ranging from 30 to 50 µm.[14,20,31–37] We selected 50 µm as the upper limit in order to also capture HRF that may be aggregated into hyper-reflective objects larger than 30 µm.

Dataset and Annotation. SD-OCT volumes (Spectralis) from BOULEVARD were selected post hoc and annotated on the B-scan level by two trained readers from the Liverpool Ophthalmic Reading Centre. Each B-scan was annotated by a single grader. In cases that presented uncertainty at initial grading, the image was referred to a senior clinician for adjudication, who made a final decision. Per volume, 2 to 9 B-scans were annotated by overlaying ellipses over HRF up to 50 µm in diameter, and manually outlining larger objects of intraretinal hyper-reflective material (IHRM). Owing to the transverse resolution of 14 µm on SD-OCT, objects smaller than 20 µm were not annotated, due to the difficulty in differentiation. The following retinal-layer boundaries were also annotated, using single lines across each B-scan: internal limiting membrane (ILM), boundary of outer plexiform layer-Henle's fiber layer (OPL-HFL), and center of RPE. Per protocol, annotations were only performed for objects with similar reflectivity as RPE.

Postprocessing of Annotations. Ellipses, shapes, and boundaries drawn on the B-scans were stored in raster format, then converted to label maps of the original image dimension. Disrupted layers were filtered out. Subsequently, ellipses were shrunk to the most hyper-reflective center using adaptive thresholding,[38] and combined with the IHRM shapes to form a single label of hyper-reflective material. For the layers, each space between a pair of adjacent boundaries was filled with a distinct label.

Model Training. The BOULEVARD study data were split on the patient level into training (1355 B-scans) and validation (155 B-scans) sets. Training images and corresponding annotation masks were used to train the algorithm to recognize HRF and IHRM. Specifically, the multiclass U-Net,[39] a convolutional neural network for biomedical image segmentation, was trained for pixel-level semantic segmentation using 250 epochs, categorical Sørensen–Dice coefficient scores loss,[40] and the Adam optimizer.[41] Similarly, the layers were trained with 50 epochs.

Postprocessing of Predictions. Objects detected by the model were categorized on the B-scan level by fitting an ellipse to each object (Supplementary Fig. S2), and those below 50 µm in diameter (long axis) were classified as HRF,

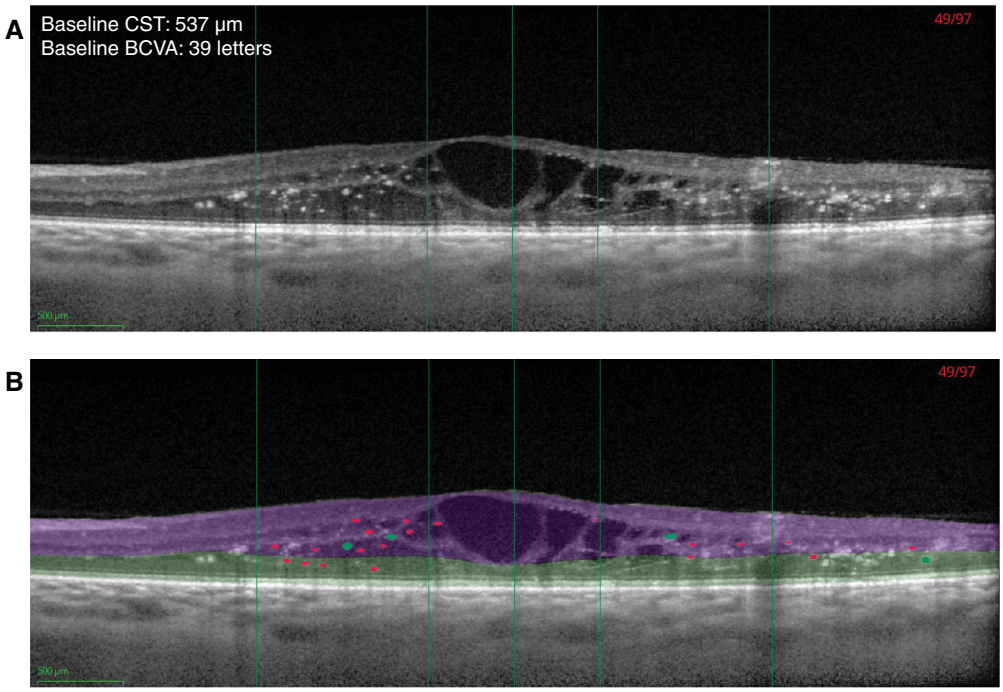

Figure 1. Example of automated hyperreflective foci (HRF) segmentation. Example spectral-domain optical coherence tomography image from one patient (age 67 years, female) at baseline (**A**) without and (**B**) with segmentation of layers, HRF (*red*; ≤50 µm), and larger intraretinal hyper-reflective objects (*green*; >50 µm and ≤100 µm). The algorithm filtered out objects >100 µm; hence, these objects are not colored in the figure. Early Treatment Diabetic Retinopathy Study rings are indicated with *green vertical lines* (*center*, 1- and 3-mm–diameter rings). Inner retina (between the internal limiting membrane and the outer plexiform layer-Henle's fiber layer [OPL-HFL]; *purple*) and outer retina (between the OPL-HFL and the retinal pigment epithelium; *green*). BCVA, best-corrected visual acuity; CST, central subfield thickness.

with the remainder discarded. A subset of HRF predictions was reviewed by two clinicians with expertise in retinal imaging (authors I.B. and C.G.) to ensure that no noise was classified as HRF. Predicted layers were converted back to layer boundaries and stored in elevation-map format. Continuous layers were predicted regardless of potential disruptions. Example scans showing the automated prediction of HRF and layers are shown in Figure 1.

Feature Extraction. Using the B-scan-level predictions, two types of features were automatically extracted on the SD-OCT-volume level: counts of distinct HRF objects across B-scans, and total HRF volume. Slice thickness, that is, the space between the centers of two adjacent B-scans, was used as depth information to calculate volumes.

HRF counts and volumes were assessed in the 1-mm and 3-mm Early Treatment Diabetic Retinopathy Study (ETDRS) rings, which were also separated into the inner and outer retina. The inner retina was defined as ILM to OPL-HFL, and the outer retina as OPL-HFL to RPE. The total retina was defined as ILM to RPE. We excluded the 6-mm diameter from the analysis due to significant variability in the scan area for Spectralis volume scans, despite identical parameter settings. This variability may lead to incomplete data at the perimeter, thus potentially making volume-wide measurements unreliable.

Model Validation. Model performance for HRF and IHRM was evaluated against the annotations on the validation set using Dice scores,[42,43] measuring the overlap between annotations and model predictions, as well as volume difference, sensitivity, and specificity. Performance for layers was evaluated using Chamfer distance,[44] which measures the average distance (in pixels) between the annotated and predicted elevation of layers across A-scans.

Co-Localization of HRF and Cystoid IRF

Overview. Co-localization of HRF with cystoid IRF was assessed within the 3.0-mm diameter ETDRS ring by comparing the spatial distribution of each biomarker in the en face projection of the SD-OCT volumes. Cystoid IRF was segmented using a deep-learning–based algorithm developed for the quantification of IRF and SRF.[45] To ensure the presence of a significant volume of HRF, enabling the assessment of a potential correlation, analysis was limited to the top 10% of volume scans that contained the greatest HRF volumes at baseline ($n = 159$).

En Face Projection. IRF and HRF of the selected volumes were projected onto the en face plane (Fig. 2). To render distributions of IRF (cystoid pockets) and HRF (individual small objects) comparable and increase the robustness of the co-localization, Gaussian blurring was applied to the en face projections of both HRF and cystoid IRF to ensure a more stable and comparable result.

Statistical Analysis

Prior to feature extraction and statistical analysis, HRF had been prespecified as a biomarker of interest. Baseline HRF volume distributions were assessed in a treatment-agnostic manner by pooling all treatment arms and splitting the data into quartiles for BCVA (quartile 1: ≤57 letters; quartile 2: 58 to 65 letters; quartile 3: 66 to 70 letters; and quartile 4: >70 letters), central subfield thickness (CST) measured from ILM to Bruch's membrane (quartile 1: ≤382 µm; quartile 2: >382 µm and ≤455 µm; quartile 3: >455 µm and ≤552 µm; and quartile 4: >552 µm), and cystoid IRF volume (1-mm–diameter ETDRS ring [quartile 1: ≤60,040 pL; quar-

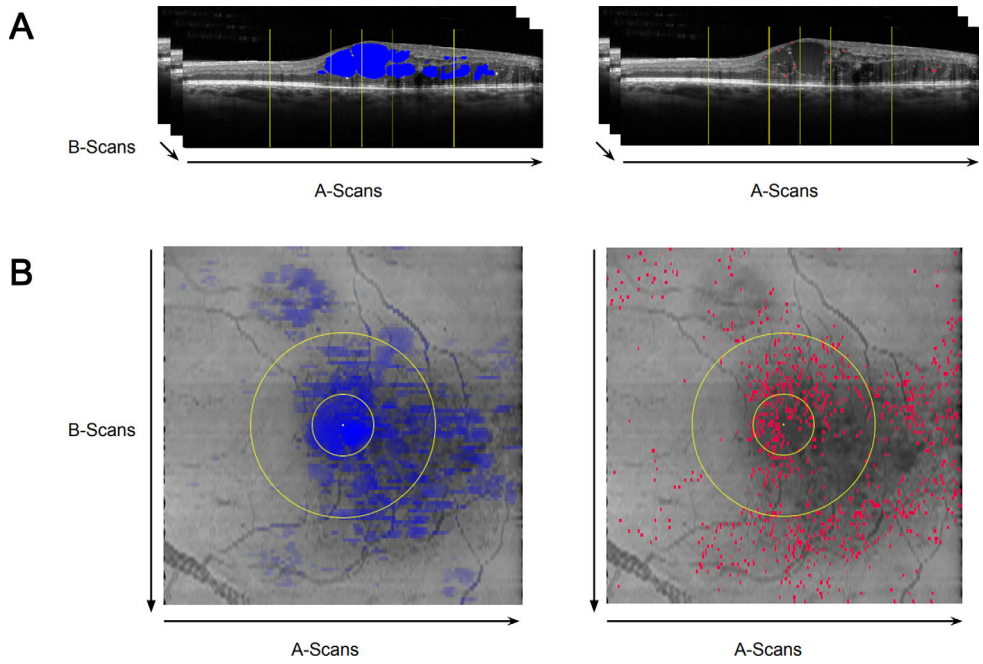

Figure 2. (**A**) Volumetric segmentation and (**B**) en face projection of intraretinal fluid (IRF [*blue*]; *first column*) and hyper-reflective foci (HRF [*red*]; *second column*). The opacity of the segmented pixels in the projection is proportional to the height of the IRF in that location (i.e. a brighter color indicates a greater IRF thickness).

tile 2: >60,040 pL and ≤106,250 pL; quartile 3: >106,250 pL and ≤166,349 pL; and quartile 4: >166,349 pL], 3-mm–diameter ETDRS ring [quartile 1: ≤216,903 pL; quartile 2: >216,903 pL and ≤409,728 pL; quartile 3: >409,728 pL and ≤671,259 pL; and quartile 4: >671,259 pL]).

To assess HRF volume distribution by disease severity, Diabetic Retinopathy Severity Score (DRSS) levels were grouped as follows: (1) diabetic retinopathy (DR) absent or questionable (DRSS 10 to 20); (2) mild and moderate nonproliferative DR (NPDR; DRSS 35 and 43); (3) moderately severe, severe, and very severe NPDR (DRSS 47 and 53); and (4) mild, moderate, and high-risk proliferative DR (PDR; DRSS 60 to 85).

Statistical significance of differences between the quartiles described above was assessed using Kruskal-Wallis tests, followed by pairwise comparison using Wilcoxon Rank Sum tests. Co-localization of HRF and cystoid IRF, as well as the null hypothesis with IRF, were evaluated using Pearson's correlation.

No adjustment to the significance level was made to account for multiple treatment comparisons or analyses at multiple time points; *P* values are nominal and should be interpreted in an exploratory context.

For IRF and HRF co-localization, a null hypothesis of HRF distribution, as well as three alternative distributions informed by statistical variables, were generated as comparators, each with the equivalent number of objects as measured in the actual HRF distribution. The null hypothesis consisted of a uniform distribution of dots. The three alternative distributions were: (1) a Gaussian distribution with the same mean as the observed HRF distribution, and axis-specific standard deviations equal to the observed HRF standard deviations; (2) a Gaussian distribution with the same mean as the observed HRF distribution, but with a uniform standard deviation; and (3) a Gaussian distribution with a mean equal to the center of the image, and with a uniform standard deviation.

Results

Good Performance of HRF Segmentation Algorithm

The performance of the HRF segmentation algorithm was assessed using the validation set of manually annotated B-scans. Median and average Dice scores on the validation set were 71% and 65%, respectively, which are considered to be good scores, given the variability of Dice scores for small-size objects, such as HRF.[46] Median and average specificity on the validation set were 76% and 69%, respectively. We also compared median and average ground-truth volumes on the B-scan level with the segmented volumes in the validation set. These were 30 and 50 nL for the ground-truth volumes, respectively, and 20 and 40 nL for the segmented volumes, respectively. A scatter plot comparing ground-truth and segmented volumes is shown in Figure 3, with the corresponding Bland Altman plot.

To assess layer-segmentation performance, Chamfer distances were calculated, which measure the distance in pixels between two objects. The median (standard error) Chamfer distances across B-scans in the validation set for ILM, OPL-HFL, and RPE were −0.98 (0.05), 0.53 (1.66), and −1.0 (0.08) pixels, respectively, which are below the optical resolution of SD-OCT machines. Boxplots are shown in Supplementary Figure S4.

In DME, HRF Are Almost Universally Present at Baseline

At baseline, prior to treatment initiation, the quantitative assessment of HRF volumes and counts in SD-OCT volume

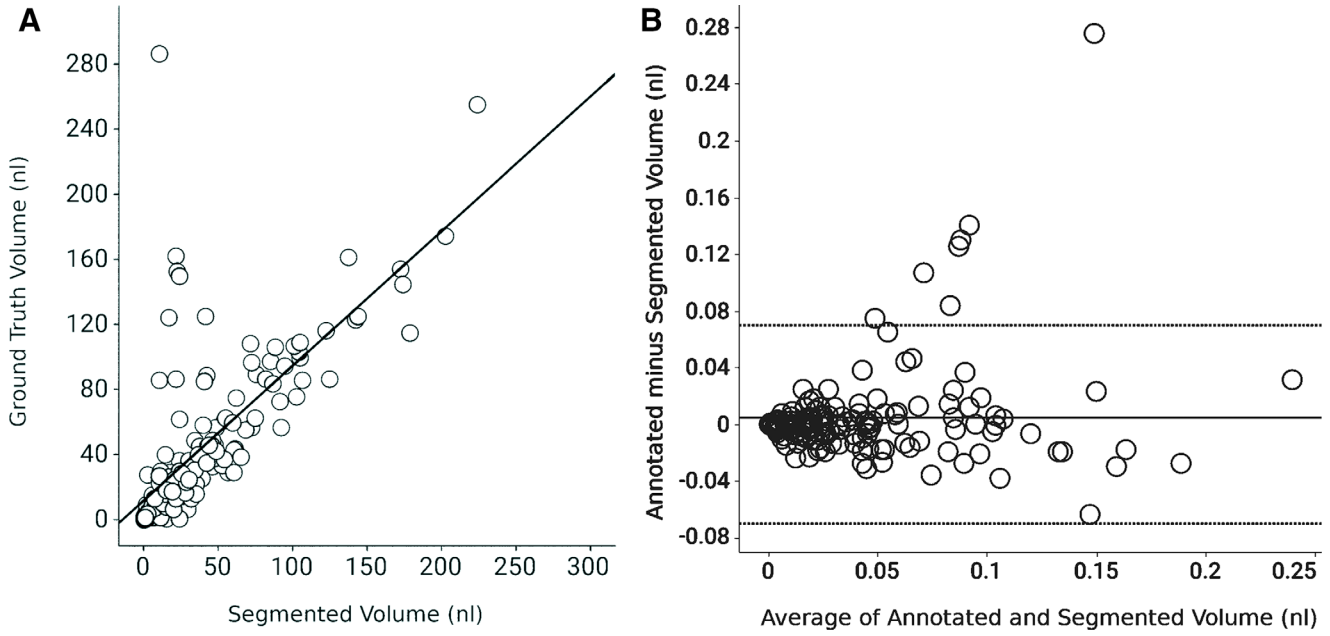

Figure 3. (**A**) Scatterplot of holdout ground-truth versus segmented hyper-reflective foci and intraretinal hyper-reflective material volumes, including a linear best-fit line. The outliers on the *top left* of the scatterplot, which are not detected by the segmentation model, represent large objects less hyper-reflective than the retinal pigment epithelium (e.g. see Supplementary Fig. S3). (**B**) Bland Altman plot of holdout ground-truth versus segmented hyper-reflective foci and intraretinal hyper-reflective material volumes. As estimated by bootstrapping (1000 repetitions), the mean value for annotated minus segmented volume (y axis) was at 0.0047 nl (95% CI = −0.0009 to 0.0103). The upper limit of agreement (LOA) was at 0.0777 nl (95% CI = 0.0489 to 0.1065) and the lower LOA was at −0.0683 nl (95% CI = −0.0395 to 0.0971).

Table 1. HRF Volume, Count, and Presence at Baseline

Location	Measure	Pooled Treatment Groups
Inner retina, 1 mm	Median (IQR) volume, pL	126.0 (270.2)
	Median (IQR) count	5.0 (8.0)
	HRF present	1369/1527 (89.7%)
Inner retina, 3 mm	Median (IQR) volume, pL	825.4 (1443.4)
	Median (IQR) count	29.0 (43.0)
	HRF present	1520/1527 (99.5%)
Outer retina, 1 mm	Median (IQR) volume, pL	69.2 (201.7)
	Median (IQR) count	3.0 (6.0)
	HRF present	1189/1527 (77.9%)
Outer retina, 3 mm	Median (IQR) volume, pL	784.6 (1930.4)
	Median (IQR) count	26.0 (56.0)
	HRF present	1489/1527 (97.5%)
Total retina, 1 mm	Median (IQR) volume, pL	242.5 (454.7)
	Median (IQR) count	9.0 (14.0)
	HRF present	1455/1527 (95.3%)
Total retina, 3 mm	Median (IQR) volume, pL	1964.3 (3325.2)
	Median (IQR) count	64.0 (96.0)
	HRF present	1523/1527 (99.7%)

HRF, hyper-reflective foci; IQR, interquartile range; pL, picoliters; 1 mm, 1-mm diameter Early Treatment Diabetic Retinopathy Study (ETDRS) ring; 3 mm, 3-mm diameter ETDRS ring.

scans showed that HRF are almost universally present (up to 99.7%) within the retinas of patients with DME. Specifically, looking at the central subfield, 89.7% of patients had HRF in the inner retina, and 77.9% in the outer retina. For the central 3-mm diameter, 99.5% had HRF in the inner retina, and 97.5% in the outer retina (Table 1). Few to none were detected in an external control group of patients without retinal conditions (inner and outer retina at both diameters; unpublished data). An example SD-OCT scan with and without HRF segmentation is shown in Figure 1. The baseline demographic and ocular characteristics of the patients included in this analysis are shown in Table 2.

HRF Distribution Inner Versus Outer Retina and 1-mm Versus 3-mm–Diameter ETDRS Ring

HRF counts and volumes at baseline were non-normally distributed for both ETDRS diameters and both retinal locations (Supplementary Fig. S5). Median (interquartile range [IQR]) HRF volumes and counts are shown in Table 1.

Within the central subfield, approximately double the volume of HRF was observed in the inner retina (median = 126.0, IQR = 270.2 pL) versus the outer retina (median = 69.2, IQR = 201.7 pL). Conversely, in the 3-mm–diameter ETDRS ring, similar HRF volumes were measured in the inner (median = 825.4, IQR = 1443.4 pL) and outer retina (median = 784.6, IQR = 1930.4 pL). Similar ratios were also observed for HRF counts (Table 3).

Greater Median HRF Volumes Were Seen With Increasing CST, Cystoid IRF Volume, and Disease Severity, and With Lower BCVA Score

In order to assess HRF distributions in the total retina (i.e. inner and outer retina combined) in relation to several disease parameters, patients were split into quartiles of BCVA, CST, and cystoid IRF volume, and by the four DRSS severity groups (Fig. 4). For BCVA, higher median HRF volumes were seen with decreasing BCVA score in the 3-mm–diameter ETDRS ring (nominal $P = 0.0109$), but not in the 1-mm diameter ring where median HRF volumes were

Table 2. Baseline Demographic and Ocular Characteristics

Characteristic	Pooled Treatment Groups ($N = 1527$)
Age, y, mean (SD)[*]	62.1 (9.8)
Sex, *n* (%)	
Female	606 (39.7%)
Male	921 (60.3%)
Geographic region, *n* (%)	
United States and Canada	785 (51.4%)
Asia[†]	167 (10.9%)
Rest of the world[‡]	575 (37.7%)
Race, *n* (%)[§]	
White	1185 (77.6%)
Asian	142 (9.3%)
Black or African American	116 (7.6%)
American Indian or Alaska Native	18 (1.2%)
Native Hawaiian or other Pacific Islander	6 (0.4%)
Hispanic or Latinx	275 (18.0%)
Nonocular characteristics	
BMI, kg/m^2, mean (SD)	30.8 (6.46)
HbA1c, %, mean (SD)	7.6 (1.14)
Type 2 diabetes, *n* (%)	1443 (94.5)
Systolic blood pressure, mm Hg, mean (SD)	137.3 (15.80)
Ocular characteristics	
BCVA (ETDRS letters), mean (SD)	62.2 (9.5)
CST, µm, mean (SD)	479.3 (128.4)
Macular ischemic nonperfusion, *n* (%)	630 (44.6)
Macular leakage, *n* (%)	1459 (99.9)
Time since DME diagnosis (months), mean (SD)	18.2 (32.3)
Anti-VEGF treatment naïve, *n* (%)	1198 (78.5)
Previously anti-VEGF treated, *n* (%)	329 (21.5)
Time since last anti-VEGF treatment (months), mean (SD)	18.6 (18.09)
Phakic, *n* (%)	1143 (74.9)
ETDRS-DRSS status, *n* (%)[‖]	
DR absent/questionable (ETDRS-DRSS level 10/12, 14/20)	39 (2.6%)
Mild to moderate NPDR (ETDRS-DRSS level 35, 43)	816 (53.8%)
Moderately severe to very severe NPDR (ETDRS-DRSS level 47, 53)	515 (34.0%)
PDR (ETDRS-DRSS level 61, 65, 71/75)	121 (8.0%)
Cannot grade (ETDRS-DRSS level 90)	25 (1.6%)

BCVA, best-corrected visual acuity; BMI, body mass index; CST, central subfield thickness; DME, diabetic macular edema; DR, diabetic retinopathy; DRSS, Diabetic Retinopathy Severity Scale; ETDRS, Early Treatment Diabetic Retinopathy Study; HbA1c, glycated hemoglobin; NPDR, nonproliferative diabetic retinopathy; PDR, proliferative diabetic retinopathy; SD, standard deviation; VEGF, vascular endothelial growth factor.

[*] Age at randomization.

[†] Asia includes China, Hong Kong, Japan, Singapore, South Korea, Taiwan, and Thailand.

[‡] Rest of the world includes Argentina, Australia, Austria, Belgium, Brazil, Bulgaria, Czech Republic, Denmark, France, Germany, Hungary, Israel, Italy, Mexico, The Netherlands, New Zealand, Peru, Poland, Portugal, Russia, Slovakia, South Africa, Spain, Switzerland, Turkey, Ukraine, and the United Kingdom.

[§] Not all race categories are listed; therefore, the sum of proportions shown may not equal 100%.

[‖] $N = 1516$.

largely comparable across quartiles (nominal $P = 0.3633$; see Figs. 4A, 4B). For CST, increasing median HRF volumes were observed with increasing retinal thickness in the 3-mm–diameter ring (nominal $P < 0.0001$). Similar results were seen in the 1-mm–diameter ring (nominal $P < 0.0001$), with the exception of the last quartile, which was slightly lower (see Figs. 4C, 4D). Greater cystoid IRF volumes corresponded to greater median HRF volumes in the 3-mm–diameter ring (nominal $P < 0.0001$), and in the 1-mm–diameter ring but to a lesser extent (nominal $P < 0.0001$; see Figs. 4E, 4F). In both the 1- and 3-mm diameter rings, median HRF volumes were higher with increasing disease severity except in eyes with PDR (see Figs. 4G, 4H), in which marginally lower median HRF volumes were found. A similar pattern was observed when assessing the distribution of CST measurements in the same four DRSS groups (see Fig. 4I).

Table 3. Ratios (Inner/Outer Retina) of HRF Count and Volume

	Median HRF Volume (pL)		Median HRF Count	
	1-mm Ring	3-mm Ring	1-mm Ring	3-mm Ring
Inner retina	126.0	825.4	5.0	29.0
Outer retina	69.2	784.6	3.0	26.0
Ratio	1.8	1.1	1.7	1.1

Ratio is calculated as value for inner retina/value for outer retina. HRF, hyper-reflective foci; 1-mm ring, 1-mm–diameter Early Treatment Diabetic Retinopathy Study (ETDRS) ring; 3-mm ring, 1-mm–diameter ETDRS ring; pL, picoliters.

HRF and Cystoid IRF Co-Localize in the En Face Projection of the SD-OCT Volume

We looked at HRF and IRF co-localization in the en face projection within the 3-mm–diameter ETDRS ring (see Fig. 2). In order to ensure the presence of a significant volume of HRF to effectively test the hypothesis that HRF and IRF co-localize, the analysis was performed using the top 10% of volume scans that contained the greatest HRF volumes at baseline ($n = 159$). Examples of the distribution of HRF and cystoid IRF in en face images are shown in Figure 5, in which both fovea-centered and off-center HRF distributions are visible. The null hypothesis that HRF are distributed randomly across the imaged area was comprehensively rejected ($r = 0.00$). The IRF coordinates correlated more strongly with the measured HRF coordinates (mean $r = 0.33$) than with the three alternative, artificial HRF distributions, with mean r values of 0.19, 0.18, and 0.14 for alternative distribution 1, 2, and 3, respectively. In addition, the small difference between alternative distributions 1 and 2 versus the larger difference between alternative distributions 2 and 3 indicate that the removal of shape-of-distribution information has a lesser impact compared to removing the information regarding the HRF's distribution's center of gravity. Thus, the analysis showed that HRF and cystoid IRF co-localize in the en face view.

Discussion

In DME, HRF represent a potential biomarker for disease severity and progression.[12–15] The aim of this post hoc analysis was to assess the baseline distribution of HRF within the retina, and whether HRF co-localize with cystoid IRF in patients with DME. The large data set, the fully automated detection and volumetric quantification of HRF, and the objective nature of the algorithmic approach make this a robust analysis of a potentially key biomarker in DME.

Investigative Ophthalmology & Visual Science

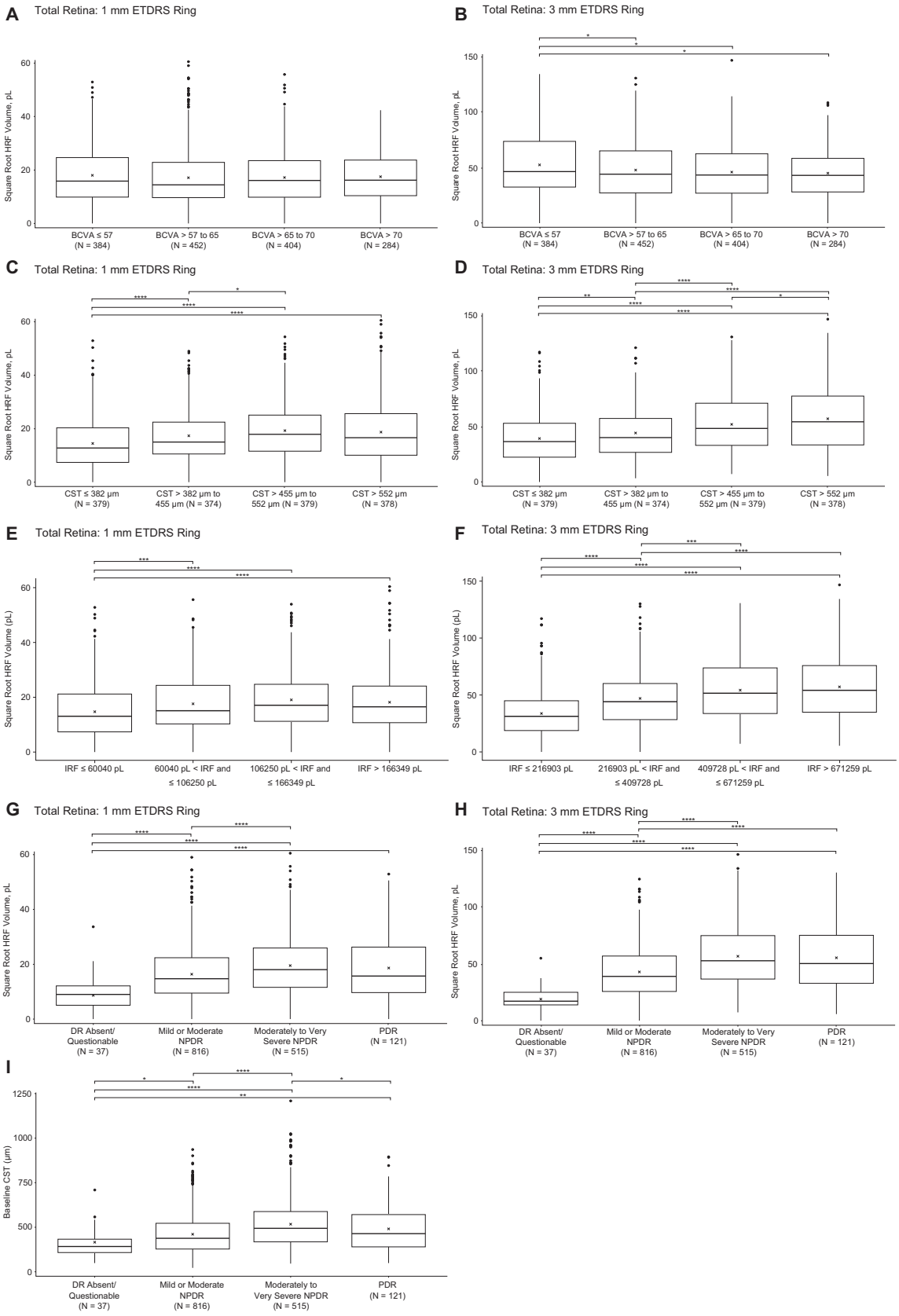

Figure 4. Baseline hyper-reflective foci (HRF) distribution in the total retina (i.e. inner and outer retina combined) in the 1-mm– and 3-mm–diameter Early Treatment Diabetic Retinopathy Study (ETDRS) rings by quartiles of (**A, B**) best-corrected visual acuity (BCVA), (**C, D**) central subfield thickness (CST), and (**E, F**) intraretinal fluid (IRF), as well as (**G, H**) groups of Diabetic Retinopathy Severity Score (DRSS). In addition, (**I**) shows CST distribution by DRSS groups. Nominal *P* values, derived from pairwise Wilcoxon Rank Sum tests, are indicated as: **P* ≤ 0.05, ***P* ≤ 0.01, ****P* ≤ 0.001, *****P* ≤ 0.0001.

Investigative Ophthalmology & Visual Science

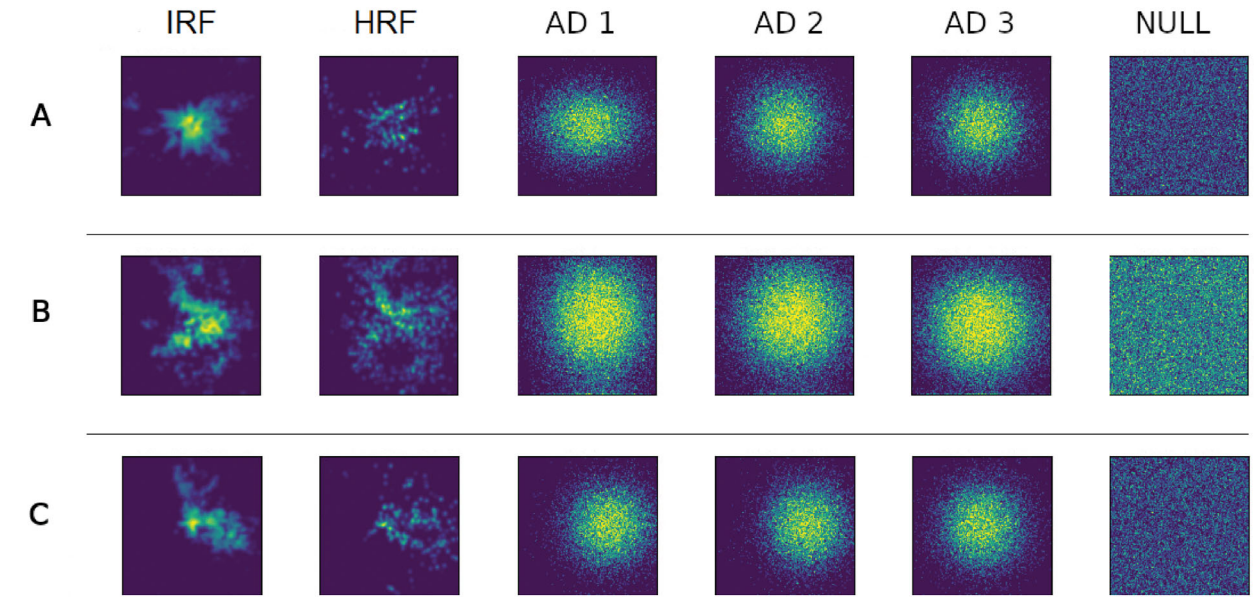

Correlation to IRF coordinates	Actual HRF	AD 1	AD 2	AD 3	NULL
Mean (SD) r-value	0.33 (0.14)	0.19 (0.08)	0.18 (0.08)	0.14 (0.07)	0.00 (0.00)

Figure 5. Correlation of hyper-reflective foci (HRF) and intraretinal fluid (IRF) coordinate distributions in the en face projection of SD-OCT volumes (upper 10% of the data distribution for baseline HRF volume). Three example cases (one row per case) of HRF and IRF co-localization in the en face projection are shown. The observed distributions for IRF (*first column*) and HRF (*second column*), the alternative artificial distributions (AD; *columns 3–5*), and the artificially generated null hypothesis of HRF distribution (*column 6*) are shown. AD 1: Gaussian distribution with mean and standard deviations (SD) equal to the observed HRF distribution; AD 2: as for AD 1, but with uniform SD equal to the mean of SDs along the 2 axes; AD 3: as for AD 2, but with mean equal to the center of the image; NULL: uniform distribution. *Below*: Mean and SD of Person's correlation *r* values obtained from comparison of IRF coordinates to the actual HRF distribution, as well as to the four hypotheses.

Past publications on intraretinal HRF in DME have relied on manual counting, which has inherent limitations: manual HRF assessments are often limited to a subset of scans and not the entire SD-OCT volume, assessments of HRF are performed in a small number of patients due to the laborious nature of manual counting, and HRF cannot be assessed volumetrically. As seen in Figure 5, HRF distributions are not necessarily centered on the fovea, thus assessing only a subset of central B-scans does not provide a reliable representation of HRF load. The discrepancies seen in the literature regarding HRF presence or count as a predictor of vision outcomes[27] may be due to the biases introduced by manual counting. Another factor that makes comparison of past studies challenging is the use of variable HRF definitions, which are not consistently reported.[27]

The use of artificial intelligence to automate HRF quantification eliminates such biases, by enabling rapid, objective, and comprehensive assessment of all B-scans within the SD-OCT volume, thus making it possible to perform a robust analysis with large patient numbers, consistent identification of HRF based on the grading criteria selected, and extraction of volumetric HRF data. Nevertheless, comparison of analyses performed by different algorithms will remain challenging for as long as no consensus definition of HRF has been reached in regard to size, back shadowing, location, and relative reflectivity. Here, we have presented a deep-learning–based algorithm with a robust performance for the segmentation of HRF in DME. We used a combination of DICE score, absolute volume difference, sensitivity, and specificity for model validation on the holdout set. The specificity metric, together with expert review of algorithm output, ensured that the model did not detect noise. A limitation of the current algorithm is that it cannot track individual objects in a full three-dimensional segmentation; this would require denser B-scans to achieve better resolution. Nevertheless, to the best of our knowledge, this is the first time that a volumetric assessment of HRF in DME has been performed on images from a large clinical trial data set, thus providing a reference for future studies of this nature. However, the algorithm will require testing and validation prior to its application to images from acquisition systems other than the Spectralis.

As the regions defined by the 1 and 3 mm ETDRS circles on the retina may vary due to variability in eye axial length in the sample, a weakness of the current approach is the potential for volume measurement errors arising due to the lack of axial length information for correct lateral scaling of the OCT scans.[47] This may have resulted in apparent differences between individuals that may not have been true differences. As noted by Llanas and colleagues in their systematic review on correcting of OCT image scaling,[47] "while many devices report scan dimensions in absolute retinal distance units (millimeters), few disclose the axial length of the model eye assumed by their system (which

varies across manufacturers)." This issue warrants further investigation.

Our analysis showed that at baseline, HRF are almost universally present in eyes with DME (up to 99.7% depending on ETDRS ring and retinal location). This is in accord with previous reports on the prevalence of HRF, where approximately 90% of eyes with DME were shown to exhibit this feature on SD-OCT.[13,48] Although the quantity of HRF in the inner versus outer retina was comparable in the 3-mm diameter, twice as many HRF were present in the inner retina of the central subfield compared with the outer retina. This imbalanced distribution may suggest a greater rate of HRF removal in the outer retina of the central subfield, or may be due to the topography of Henle's fiber layer in the central subfield.

We observed higher HRF volumes with increasing DRSS, CST, and cystoid IRF. Furthermore, we noted a trend for worse BCVA with greater HRF volumes. These findings suggest that HRF are markers for disease severity. However, the median HRF volume, as well as the median CST, was slightly lower in eyes with PDR than with severe NPDR. This may be due to one third of study eyes in the PDR group (33 out of 121) receiving panretinal photocoagulation (PRP) more than 3 months prior to study enrollment (PRP within 3 months of enrollment was a study exclusion criterion), an intervention known to cause retinal thinning and result in reduced severity of retinopathy. Consequently, prior PRP may have confounded the relationship between DR severity and HRF in study eyes with PDR.

In addition to the above-mentioned potential relationship between cystoid IRF and HRF volumes, the shape distribution of HRF in the en face projection of SD-OCT volumes followed the distribution of cystoid IRF. This finding is in line with that reported by Kashani et al.,[25] who showed co-localization with intraretinal hyper-reflective material, in particular hyper-reflective fluid. We recognize that the correlation between HRF distribution and IRF localization is modest; however, given that the shape distribution of the former follows that of the latter, we therefore believe that these OCT features are linked and hypothesize that the HRF in DME may originate within IRF cysts. Further exploration is warranted to determine the exact location of and relationship between HRF and IRF cysts, including an assessment of co-localization in three dimensions and over time.

In addition to the null hypothesis, alternative, artificial HRF distributions were generated to reflect the statistical characteristics of the actual HRF distribution to varying degrees. The correlation coefficients of these artificial HRF distributions in comparison to cystoid IRF were lower, and reduced as the artificial HRF distributions became less characteristic of the actual HRF distribution. Thus, artificial HRF distributions that mimicked the actual HRF distribution less stringently correlated less with cystoid IRF. Comparison of the three artificial HRF distributions showed that IRF and HRF were quite often located off-center in relation to the fovea, and that, on average, the shape of the IRF and HRF distribution had no distinct pattern.

In conclusion, our analysis showed that HRF are almost universally present within the retina of DME patients, and may be linked to disease severity, thus highlighting them as a potential biomarker of interest in this condition. For future studies, we recommend the use of automated approaches to analyze full SD-OCT volume scans to minimize bias. Whereas volumetric analyses constitute the most robust approach, incorporating size differences into the measure, similar results can also be obtained with the more tangible measure of HRF counts, providing the number of B-scans is consistent throughout the study population. Because the link with measures of disease severity is greater in the 3-mm–diameter ETDRS ring, this may be the more relevant area of assessment.

Acknowledgments

The authors thank the Liverpool Ophthalmic Reading Centre graders and expert clinicians for their expertise and support in their work on image annotations.

Supported by F. Hoffmann-La Roche Ltd. (Basel, Switzerland). The sponsor participated in the design of the study; collection, management, analysis, and interpretation of the data; preparation, review, and approval of the manuscript.

Meeting Presentation: Data reported in this manuscript were presented in part at the Association for Research in Vision and Ophthalmology Annual Meeting, April 2023, New Orleans, Louisiana.

Disclosure: **E.L. von Schulthess**, F. Hoffmann-La Roche Ltd. (E), F. Hoffmann-La Roche Ltd. (I); **A. Maunz**, F. Hoffmann-La Roche Ltd. (E); **U. Chackravarthy**, Apellis (C), Boehringer Ingelheim (C), Iveric Bio (C), Roche (C), Adverum (R), Oxurian (R); **N. Holekamp**, Apellis (C), Bayer (C), Biogen (C), Boehringer (C), Cardinal (C), Clearside Biosciences (C), EyePoint Pharmaceuticals (C), Genentech, Inc. (C), Gyroscope (C), Medpace (C), Medscape (C), Notal Vision (C), Novartis (C), Regeneron (C), Roche (C), Stealth Biosciences (C), Vial (C), Gemini (F), Genentech, Inc. (F), Gyroscope (F), Notal Vision (F), Editas (R), Ocuphire (R), Roche (R), Apellis (I), Nacuity (I), Notal Vision (I), Roche (E); **D. Pauleikhoff**, Apellis (C), Novartis (C), Bayer (C), Roche (C), Heidelberg Engineering (C); **K. Patel**, F. Hoffmann-La Roche Ltd. (E), F. Hoffmann-La Roche Ltd. (I); **I. Bachmeier**, F. Hoffmann-La Roche Ltd. (E), F. Hoffmann-La Roche Ltd. (I); **S. Yu**, F. Hoffmann-La Roche Ltd. (E); **Y. Cohen**, F. Hoffmann-La Roche Ltd. (E), F. Hoffmann-La Roche Ltd. (I); **M.P. Scherb**, F. Hoffmann-La Roche Ltd. (E), F. Hoffmann-La Roche Ltd. (I); **I.L. Jones**, F. Hoffmann-La Roche Ltd. (E), F. Hoffmann-La Roche Ltd. (I); **K. Gibson**, F. Hoffmann-La Roche Ltd. (E), F. Hoffmann-La Roche Ltd. (I); **J.R. Willis**, Genentech, Inc. (E); **C. Glittenberg**, F. Hoffmann-La Roche Ltd. (E), F. Hoffmann-La Roche Ltd. (I); **R.P. Singh**, Alcon (C), Alimera (C), Apellis (C), Bausch + Lomb (C), Carl Zeiss (C), Coherus (C), EyePoint Pharmaceuticals (C), Genentech, Inc. (C), Gyroscope (C), Iveric Bio (C), Novartis (C), Regeneron (C); **S. Fauser**, F. Hoffmann-La Roche Ltd. (E), F. Hoffmann-La Roche Ltd. (I)

References

1. Bandello F, Parodi MB, Lanzetta P, et al. Diabetic macular edema. *Macular Edema*. 2017;58:102–138.
2. Daruich A, Matet A, Moulin A, et al. Mechanisms of macular edema: beyond the surface. *Prog Retin Eye Res*. 2018;63:20–68.
3. Chauhan MZ, Rather PA, Samarah SM, Elhusseiny AM, Sallam AB. Current and novel therapeutic approaches for treatment of diabetic macular edema. *Cells*. 2022;11(12):1950.
4. Vujosevic S, Simó R. Local and systemic inflammatory biomarkers of diabetic retinopathy: an integrative approach. *Invest Ophthalmol Vis Sci*. 2017;58(6):BIO68–BIO75.
5. Rübsam A, Parikh S, Fort PE. Role of inflammation in diabetic retinopathy. *Int J Mol Sci*. 2018;19(4):942.

6. Mesquida M, Drawnel F, Fauser S. The role of inflammation in diabetic eye disease. *Semin Immunopathol*. 2019;41(4):427–445.
7. Kolomeyer AM, Eichenbaum DA, Kiernan DF, Suñer IJ, Hariprasad SM. The 0.19-mg fluocinolone acetonide implant for the treatment of diabetic macular edema: an expert consensus. *Ophthalmic Surg Lasers Imaging Retina*. 2023;54(3):166–173.
8. Virgili G, Parravano M, Evans JR, Gordon I, Lucenteforte E. Anti-vascular endothelial growth factor for diabetic macular oedema: a network meta-analysis. *Cochrane Database Syst Rev*. 2018;10:CD007419.
9. Elman MJ, Aiello LP, Beck RW, et al. Randomized trial evaluating ranibizumab plus prompt or deferred laser or triamcinolone plus prompt laser for diabetic macular edema. *Ophthalmology*. 2010;117(6):1064–1077.e35.
10. Glassman AR, Wells JA, Josic K, et al. Five-year outcomes after initial aflibercept, bevacizumab, or ranibizumab treatment for diabetic macular edema (Protocol T Extension Study). *Ophthalmology*. 2020;127(9):1201–1210.
11. Bressler NM, Beaulieu WT, Glassman AR, et al. Persistent macular thickening following intravitreous aflibercept, bevacizumab, or ranibizumab for central-involved diabetic macular edema with vision impairment: a secondary analysis of a randomized clinical trial. *JAMA Ophthalmol*. 2018;136(3):257–269.
12. Fragiotta S, Abdolrahimzadeh S, Dolz-Marco R, Sakurada Y, Gal-Or O, Scuderi G. Significance of hyperreflective foci as an optical coherence tomography biomarker in retinal diseases: characterization and clinical implications. *J Ophthalmol*. 2021;2021:e6096017.
13. Zur D, Iglicki M, Busch C, et al. OCT biomarkers as functional outcome predictors in diabetic macular edema treated with dexamethasone implant. *Ophthalmology*. 2018;125(2):267–275.
14. Rübsam A, Wernecke L, Rau S, et al. Behavior of SD-OCT detectable hyperreflective foci in diabetic macular edema patients after therapy with anti-VEGF agents and dexamethasone implants. *J Diabetes Res*. 2021;2021:e8820216.
15. Chatziralli I, Theodossiadis P, Parikakis E, et al. Dexamethasone intravitreal implant in diabetic macular edema: real-life data from a prospective study and predictive factors for visual outcome. *Diabetes Ther Res Treat Educ Diabetes Relat Disord*. 2017;8(6):1393–1404.
16. Bolz M, Schmidt-Erfurth U, Deak G, Mylonas G, Kriechbaum K, Scholda C. Optical coherence tomographic hyperreflective foci: a morphologic sign of lipid extravasation in diabetic macular edema. *Ophthalmology*. 2009;116(5):914–920.
17. Zhu R, Xiao S, Zhang W, et al. Comparison of hyperreflective foci in macular edema secondary to multiple etiologies with spectral-domain optical coherence tomography: an observational study. *BMC Ophthalmol*. 2022;22(1):352.
18. Coscas G, De Benedetto U, Coscas F, et al. Hyperreflective dots: a new spectral-domain optical coherence tomography entity for follow-up and prognosis in exudative age-related macular degeneration. *Ophthalmologica*. 2013;229(1):32–37.
19. Vujosevic S, Torresin T, Bini S, et al. Imaging retinal inflammatory biomarkers after intravitreal steroid and anti-VEGF treatment in diabetic macular oedema. *Acta Ophthalmol (Copenh)*. 2017;95(5):464–471.
20. Hwang HS, Chae JB, Kim JY, Kim DY. Association between hyperreflective dots on spectral-domain optical coherence tomography in macular edema and response to treatment. *Invest Ophthalmol Vis Sci*. 2017;58(13):5958–5967.
21. Vujosevic S, Bini S, Midena G, Berton M, Pilotto E, Midena E. Hyperreflective intraretinal spots in diabetics without and with nonproliferative diabetic retinopathy: an in vivo study using spectral domain OCT. *J Diabetes Res*. 2013;2013:e491835.
22. Kaya M, Kocak N, Ozturk T, Bolluk V, Ayhan Z, Kaynak S. Intravitreal ranibizumab and dexamethasone implant injections as primary treatment of diabetic macular edema: simultaneously double protocol. *Eye*. 2021;35(3):777–785.
23. Framme C, Schweizer P, Imesch M, Wolf S, Wolf-Schnurrbusch U. Behavior of SD-OCT–detected hyperreflective foci in the retina of anti-VEGF–treated patients with diabetic macular edema. *Invest Ophthalmol Vis Sci*. 2012;53(9):5814–5818.
24. Ota M, Nishijima K, Sakamoto A, et al. Optical coherence tomographic evaluation of foveal hard exudates in patients with diabetic maculopathy accompanying macular detachment. *Ophthalmology*. 2010;117(10):1996–2002.
25. Kashani AH, Green KM, Kwon J, et al. Suspended scattering particles in motion: a novel feature of OCT angiography in exudative maculopathies. *Ophthalmol Retina*. 2018;2(7):694–702.
26. Vujosevic S, Bini S, Torresin T, et al. Hyperreflective retinal spots in normal and diabetic eyes: B-scan and en face spectral domain optical coherence tomography evaluation. *Retina Phila Pa*. 2017;37(6):1092–1103.
27. Huang H, Jansonius NM, Chen H, Los LI. Hyperreflective dots on OCT as a predictor of treatment outcome in diabetic macular edema: a systematic review. *Ophthalmol Retina*. 2022;6(9):814–827.
28. Wykoff CC, Abreu F, Adamis AP, et al. Efficacy, durability, and safety of intravitreal faricimab with extended dosing up to every 16 weeks in patients with diabetic macular oedema (YOSEMITE and RHINE): two randomised, double-masked, phase 3 trials. *Lancet*. 2022;399(10326):741–755.
29. Eter N, Singh RP, Abreu F, et al. YOSEMITE and RHINE: phase 3 randomized clinical trials of faricimab for diabetic macular edema: study design and rationale. *Ophthalmol Sci*. 2022;2(1):100111.
30. Sahni J, Patel SS, Dugel PU, et al. Simultaneous inhibition of angiopoietin-2 and vascular endothelial growth factor-A with faricimab in diabetic macular edema: BOULEVARD phase 2 randomized trial. *Ophthalmology*. 2019;126(8):1155–1170.
31. Chen NN, Chen WD, Lai CH, et al. Optical coherence tomographic patterns as predictors of structural outcome after intravitreal ranibizumab in diabetic macula edema. *Clin Ophthalmol Auckl NZ*. 2020;14:4023–4030.
32. Liu S, Wang D, Chen F, Zhang X. Hyperreflective foci in OCT image as a biomarker of poor prognosis in diabetic macular edema patients treating with conbercept in China. *BMC Ophthalmol*. 2019;19:157.
33. Kang JW, Chung H, Chan Kim H. Correlation of optical coherence tomographic hyperreflective foci with visual outcomes in different patterns of diabetic macular edema. *Retina Phila Pa*. 2016;36(9):1630–1639.
34. Ceravolo I, Oliverio GW, Alibrandi A, et al. The application of structural retinal biomarkers to evaluate the effect of intravitreal ranibizumab and dexamethasone intravitreal implant on treatment of diabetic macular edema. *Diagnostics*. 2020;10(6):413.
35. Cavalleri M, Cicinelli MV, Parravano M, et al. Prognostic role of optical coherence tomography after switch to dexamethasone in diabetic macular edema. *Acta Diabetol*. 2020;57(2):163–171.
36. Bonfiglio V, Reibaldi M, Pizzo A, et al. Dexamethasone for unresponsive diabetic macular oedema: optical coherence tomography biomarkers. *Acta Ophthalmol (Copenh)*. 2019;97(4):e540–e544.

Investigative Ophthalmology & Visual Science

37. Narnaware SH, Bawankule PK, Raje D. Short-term outcomes of intravitreal dexamethasone in relation to biomarkers in diabetic macular edema. *Eur J Ophthalmol*. 2021;31(3):1185–1191.
38. Otsu N. A threshold selection method from gray-level histograms. *IEEE Trans Syst Man Cybern*. 1979;9(1):62–66.
39. Ronneberger O, Fischer P, Brox T. U-Net: convolutional networks for biomedical image segmentation. arXiv Preprint. Published online May 18, 2015. Accessed December 12, 2022, http://arxiv.org/abs/1505.04597.
40. Zhang W, Yang G, Huang H, et al. ME-Net: multi-encoder net framework for brain tumor segmentation. *Int J Imaging Syst Technol*. 2021;31(4):1834–1848.
41. Kingma DP, Ba J. Adam: a method for stochastic optimization. arXiv Preprint. Published online January 29, 2017. Accessed December 12, 2022, http://arxiv.org/abs/1412.6980.
42. Sørenson T. A method of establishing groups of equal amplitude in plant sociology based on similarity of species content and its application to analyses of the vegetation on Danish commons. Munksgaard in Komm., Copenhagen, Denmark; 1948.
43. Sudre CH, Li W, Vercauteren T, Ourselin S, Jorge Cardoso M. Generalised Dice overlap as a deep learning loss function for highly unbalanced segmentations. In: Cardoso MJ, Arbel T, Carneiro G, et al., eds. *Deep learning in medical image analysis and multimodal learning for clinical decision support*. Lecture Notes in Computer Science. New York, NY: Springer International Publishing; 2017:240–248.
44. Stencel M, Janacek J. On calculation of Chamfer distance and Lipschitz covers in digital images; 2006. Accessed March 27, 2023, https://www.semanticscholar.org/paper/ON-CALCULATION-OF-CHAMFER-DISTANCE-AND-LIPSCHITZ-IN-Ji-Jan%C3%A1/899c135f19ec8abc8e52dce5d903e21656605134.
45. Lu H, Maunz A. Optical coherence tomography segmentation of retinal fluids using deep learning. *Invest Ophthalmol Vis Sci*. 2023;64(8):1124.
46. Asgari Taghanaki S, Abhishek K, Cohen JP, Cohen-Adad J, Hamarneh G. Deep semantic segmentation of natural and medical images: a review. *Artif Intell Rev*. 2021;54(1):137–178.
47. Llanas S, Linderman RE, Chen FK, et al. Assessing the use of incorrectly scaled optical coherence tomography angiography images in peer-reviewed studies: a systematic review. *JAMA Ophthalmol*. 2020;138(1):86–94.
48. Huang YT, Chang YC, Meng PP, et al. Optical coherence tomography biomarkers in predicting treatment outcomes of diabetic macular edema after dexamethasone implants. *Front Med*. 2022;9:852022.

Investigative Ophthalmology & Visual Science